Journal of Molecular Catalysis A: Chemical 335 (2011) 158–168

Contents lists available at ScienceDirect

Journal of Molecular Catalysis A: Chemical

journal homepage: www.elsevier.com/locate/molcata

Modified surface and bulk properties of Fe-substituted lanthanum titanates enhances catalytic activity for CO + N_2O reaction

K.K. Kartha [a], M.R. Pai [a], A.M. Banerjee [a], R.V. Pai [b], S.S. Meena [c], S.R. Bharadwaj [a,*]

[a] Chemistry Division, Bhabha Atomic Research Centre, Mumbai 400085, India
[b] Fuel Chemistry Division, Bhabha Atomic Research Centre, Mumbai 400085, India
[c] Solid State Physics Division, Bhabha Atomic Research Centre, Mumbai 400085, India

ARTICLE INFO

Article history:
Received 19 February 2010
Received in revised form 17 October 2010
Accepted 25 November 2010
Available online 9 December 2010

Keywords:
Iron substituted lanthanum titanates
Gel combustion
TPR
Mössbauer spectroscopy
CO + N_2O

ABSTRACT

Iron substituted lanthanum titanates with nominal composition $La_2Ti_{2(1-x)}Fe_{2x}O_{7-\delta}$ ($0.0 \le x \le 1.0$) samples, were synthesized by gel combustion and conventional solid state reaction. The samples have been characterized by XRD, N_2-BET, SEM, FTIR, Mössbauer spectroscopy and TPR. Catalytic activity of these samples was evaluated for a decomposition reaction of N_2O using CO. Transition from $La_2Ti_2O_7$ (layered perovskite, $A_2B_2O_7$) to single phase, $LaFeO_3$ (perovskite, ABO_3) was observed for the samples having ≥40–60% Fe content. The microstructural analysis by SEM revealed homogeneous elongated shaped rods on single phased LTOGC surface, attributed to the layered perovskite whereas spherical grains are due to single perovskite (ABO_3) phase present in LF(0.4)GC samples. Mixed phased samples showed both elongated and spherical shape particles as observed in the SEM images. Among all samples, LF(0.6)GC have shown maximum activity of 100% conversion at 395 °C for decomposition of N_2O using CO and at 325 °C for CO oxidation. The substitution-induced anionic vacancies and asymmetric environment around Fe as suggested by Mössbauer results in partially substituted, LF(0.4)GC/SS and LF(0.6)GC/SS are responsible for considerable lowering in T_{max} observed in their TPR profiles and enhanced activity for CO + N_2O reaction as compared to pristine samples.

1. Introduction

Titanates with nominal oxygen overstoichiometry are especially interesting due to their very high electronic conductivity and stability under reducing conditions. Oxides belonging to the $La_{1-x}Sr_xTiO_{3+\delta}$ system have been studied previously as anode material in SOFCs showing good performance comparable to those of the state of art materials [1,2]. The $Ln_2Ti_2O_7$ [3] is known to be effective ferromagnetic material where, Ln = La or Nd and is an ionic conductor when Ln = Y. Preliminary studies by Happel et al. [4] reported that $LaTiO_3$ is an active catalyst for the reduction of sulfur dioxide to elemental sulfur by means of carbon monoxide with minimum formation of COS. This makes it a strong candidate for a variety of applications in electrical, optical devices and as catalysts for different reactions.

$La_2Ti_2O_7$ type compounds are able to accommodate the extra oxygen beyond the parental perovskite in short-range crystallographic shears randomly distributed in the lattice which seems to affect their properties greatly [1]. $La_2Ti_2O_7$ ($A_2B_2O_7$), perovskite of layered structures built from (1 1 0) perovskite slabs differing in thickness and bounded by crystallographic shears in the perovskite [1 0 0] direction. Adjacent slabs are offset from one another by half of one TiO_6 octahedron height and the octahedron connectivity is broken at the shear interface. In reacting mixtures of La_2O_3 and TiO_2 a range of compounds is possible. In an unreduced system $La_2O_3{\cdot}TiO_2$, $La_2O_3{\cdot}2TiO_2$ and $2La_2O_3{\cdot}9TiO_2$ have been identified by MacChesney and Sauer [5]. A mixture containing a ratio of La:Ti slightly lower than unity, if undergoes complete reduction then the $La_2O_3{\cdot}2TiO_2$ crystallizes in the perovskite $LaTiO_3$ phase. Thus, lanthanum titanate comes close to meeting the requirements for the ideal cubic perovskite structure either by reducing titanium to +3 states or by creating A-site vacancies. Much of previous works lacks detailed structural characterization, and treated these as simple cubic perovskite in spite of presence of extra oxygen in these compounds. Both A and B sites in $A_2B_2O_7$ can be substituted by diverse component ions to form stable solid solutions. The formations of stable solid solutions via partial substitutions of Ti sites by Cr^{3+}, Fe^{3+} (up to 10%) and Pr^{3+}, Nd^{3+} at A sites in $La_2Ti_2O_7$ have already been reported [1,6,7] for photocatalytic reactions. However, reports where thermal reactions are studied using lanthanum titanate as catalyst are very scanty. For proper understanding of the

* Corresponding author at: Fuel Cell Materials and Catalysis Section, 3-193 H, Chemistry Division, Modular Labs, Bhabha Atomic Research Centre, Mumbai 400085, Maharashtra, India. Tel.: +91 22 25595100 (off)/25555079 (res); fax: +91 22 25505331.
E-mail address: shyamala@barc.gov.in (S.R. Bharadwaj).

1381-1169/$ – see front matter © 2010 Elsevier B.V. All rights reserved.
doi:10.1016/j.molcata.2010.11.028

temperature dependent catalytic properties of an oxide, it is important to have insight about its bulk properties that enables an oxide to qualify as a catalyst.

To develop catalytic materials that could convert N_2O, a green house gas [8] into environmentally friendly nitrogen using another exhaust gas CO, metal cation substituted samples based on lanthanum titanate, $La_2Ti_2O_7$ were prepared and their surface properties, bulk characterizations and catalytic activities as a function of x and synthetic route were studied. *In situ* FTIR studies on these oxides for CO and N_2O adsorptions to enunciate the role of carbonate formation in the mechanism of $N_2O + CO$ reactions are discussed in subsequent communications [9]. Kapteijn et al. [10] reviewed extensively a variety of catalysts, such as metal oxides, mixed metal oxides for N_2O decomposition. Transition metals and their oxides, in forms of either simple or complex oxides, have also been investigated thoroughly [11,12]. Many investigations [13–17] have been made on modification of physico-chemical properties, so as to augment the activity, selectivity and the thermal stability of a particular oxide/mixed oxide catalyst. Recently we have studied the effect of B-site substitution on thermal–physical bulk properties and reduction behavior of In_2TiO_5 viz.; $In_2Ti_{1-x}Fe_xO_{5-\delta}$, $In_2Ti_{1-x}Cr_xO_{5-\delta}$ $(0.0 \le x \le 0.02)$ mixed oxides catalysts [18]. Earlier we have reported the role of A/B site substitution on oxide reducibility, oxygen diffusivity, etc., and correlated with the catalytic activities of $Th(VO_3)_4$ and $LaMnO_3$ oxides as a function of multiple cationic substitutions, for both CO oxidation and methanol degradation [19–23].

To rule out surface area affect and investigate the role of modified bulk properties alone on activity of lanthanum titanate $La_2Ti_2O_7$, as a result of Fe^{3+}substitution, $La_2Ti_{2(1-x)}Fe_{2x}O_{7-\delta}$ samples were synthesized by conventional ceramic route. Secondly surface area was increased by preparing nanosized crystalline powders using gel combustion route. In the present report, $La_2Ti_{2(1-x)}Fe_{2x}O_{7-\delta}$ samples were synthesized by solid state and gel combustion routes. Variations in structure and powder properties as a function of synthetic route and metal ion substitution were monitored using XRD, FTIR N_2-BET and SEM. Mössbauer studies helped in determining the coordinative atmosphere around Fe in substituted samples. The effect of Fe-doping on redox behavior of $La_2Ti_{2(1-x)}Fe_{2x}O_{7-\delta}$ was monitored by temperature programmed reduction (TPR) profiles. The catalytic properties of nominal compositions $La_2Ti_{2(1-x)}Fe_{2x}O_{7-\delta}$ were evaluated for $CO + N_2O$ reaction. The catalytic activity is evaluated as a function of temperature, time and correlated with the extent of substitution. Finally, correlations between modified bulk/surface properties – enhanced catalytic activity of $La_2Ti_{2(1-x)}Fe_{2x}O_{7-\delta}$ samples were established considering the role of Fe substitution in lanthanum titanates.

2. Experimental

2.1. Preparation

Nominal compositions $La_2Ti_{2(1-x)}Fe_{2x}O_{7-\delta}$ samples $(0.0 \le x \le 1.0)$, with typical values of 0.1, 0.2, 0.4, 0.6, 0.8, and 1.0 were synthesized by two routes viz. gel combustion and solid state routes. Flow chart of step by step synthesis of $La_2Ti_{2(1-x)}Fe_{2x}O_{7-\delta}$ samples by gel combustion method using citric acid is shown in Scheme 1. The most widely used method for the preparations of polycrystalline mixed metal oxides is the solid state reaction, where stoichiometric quantities of respective oxides, La_2O_3, TiO_2 and Fe_2O_3 were mixed and ground thoroughly for at least half an hour each. The pellets were heated first at a lower temperature of 700 °C for a time period of ~90 h, followed by calcinations at 900 °C for 40 h and 1200 °C for 63 h with intermittent grindings. Final heating was carried out at a higher temperature of 1400 °C for 48 h in order to improve the crystallinity of the products obtained.

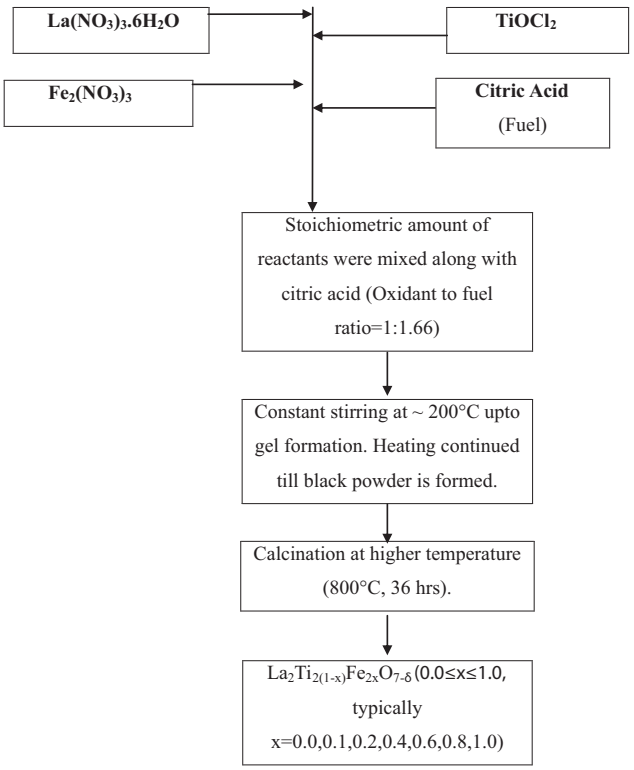

Scheme 1. Flow chart of the gel combustion synthesis.

2.2. Characterization

The powder XRD patterns were recorded on a Philips diffractometer (model PW 1710), equipped with a graphite monochromator and Ni-filtered Cu Kα radiation. The crystallite size, D, was calculated from XRD line width according to the Scherrer equation,

$$\Delta(2\theta) = \frac{K\lambda}{\beta(\cos\theta)}$$

where $\Delta(2\theta)$ is the width at half-maximum intensity (in radians) and θ is the Bragg angle of the (2 0 3) plane in the diffraction pattern of the peak, K is a constant, depending on the line shape profile (currently $K = 0.9$), λ is the wavelength of the X-ray source (in the case of Cu radiation, $\lambda = 0.154059$ nm) and β is the crystallite size in nm [19].

A Quantachrome Autosorb-1 analyzer was employed for measurement of N_2-BET surface area by recording the nitrogen adsorption isotherms. The pore size distribution and pore volume were calculated from the desorption branch using the BJH method.

The FTIR spectra of the solid samples were recorded in KBr using a JASCO FTIR (model 610) in the mid IR region (4000–400 cm^{-1}) equipped with a DTGS detector having a resolution of 4 cm^{-1}. For this purpose about 200 mg of dry KBr was mixed with 2–4% of the sample ground and pressed into a transparent, thin pellet at 5 tons/cm^2. These pellets were used for IR spectral measurements.

For microstructural examination under a scanning electron microscope (SEM) a thin layer of gold (100 Å) was coated on the sample pellets by thermal evaporation in a vacuum coating unit. A measured quantity of gold wire (99.99% pure) was wrapped on a tungsten wire which in turn was heated to evaporate the gold wire. The images of gold coated samples were recorded on scan-

Table 1
Identification of phase in nominal compositions $La_2Ti_{2(1-x)}Fe_{2x}O_{7-\delta}$ and their abbreviations.

S. no.	Nominal composition	Fe content (x)	Abbreviation LM(x)R (M = Ti/Fe, x = 0.1–1.0, R = SS/GC)	Synthesis route	Phase identification by XRD
1	$La_2Ti_2O_7$	0.0	LTOSS	SS	Single phase, $La_2Ti_2O_7$
2	$La_2Ti_{1.8}Fe_{0.2}O_{7-\delta}$	0.1	LF(0.1)SS	SS	Single phase, $La_2Ti_2O_7$
3	$La_2Ti_{1.6}Fe_{0.4}O_{7-\delta}$	0.2	LF(0.2)SS	SS	$La_2Ti_2O_7$ and $LaFeO_3$
4	$La_2Ti_{1.2}Fe_{0.8}O_{7-\delta}$	0.4	LF(0.4)SS	SS	$La_2Ti_2O_7$ and $LaFeO_3$
5	$La_2Ti_{0.8}Fe_{1.2}O_{7-\delta}$	0.6	LF(0.6)SS	SS	$LaFeO_3$
6	$La_2Ti_{0.4}Fe_{1.6}O_{7-\delta}$	0.8	LF(0.8)SS	SS	Single phase $LaFeO_3$
7	$LaFeO_3$	1.0	LFOSS	SS	Single phase $LaFeO_3$
8	$La_2Ti_2O_7$	0.0	LTOGC	GC	Single phase, $La_2Ti_2O_7$
9	$La_2Ti_{1.8}Fe_{0.2}O_{7-\delta}$	0.1	LF(0.1)GC	GC	$La_2Ti_2O_7$ and $LaFeO_3$
10	$La_2Ti_{1.6}Fe_{0.4}O_{7-\delta}$	0.2	LF(0.2)GC	GC	$La_2Ti_2O_7$ and $LaFeO_3$
11	$La_2Ti_{1.2}Fe_{0.8}O_{7-\delta}$	0.4	LF(0.4)GC	GC	Single phase $LaFeO_3$
12	$La_2Ti_{0.8}Fe_{1.2}O_{7-\delta}$	0.6	LF(0.6)GC	GC	Single phase $LaFeO_3$
13	$La_2Ti_{0.4}Fe_{1.6}O_{7-\delta}$	0.8	LF(0.8)GC	GC	Single phase $LaFeO_3$
14	$LaFeO_3$	1.0	LFOGC	GC	Single phase $LaFeO_3$

ning electron microscope Model Tescan Vega MV 2300T/40 using an accelerating voltage of 25 kV at the working distance ~10 mm.

Mössbauer spectra have been obtained using a spectrometer operated in constant acceleration mode in transmission geometry. The source employed is Co-57 in Rh matrix of strength 50 mCi. The calibration of the velocity scale is done using a α-Fe metal foil, and Mössbauer parameters are presented relative to α-Fe metal foil. The outer line width of calibration spectra was 0.29 mm s^{-1}. Mössbauer spectra were fitted by a least square fit (MOSFIT) programme assuming Lorentzian line shapes.

Temperature programmed reduction/oxidation (TPR/O) run was recorded on a TPDRO-1100 analyzer (Thermo Quest, Italy) under the flow of (H_2 (5%) + Ar) alternatively O_2 (5%) + He at a gas flow rate of 20 ml min^{-1}, in temperature range 25–1100 °C, at a heating rate of 6 °C min^{-1}. H_2O produced was removed from the evolved gases through a trap attached prior to TCD detector.

2.3. Catalytic activity

A fixed-bed continuous-flow tubular reactor made of quartz was employed for the measurement of catalytic activity of different samples for CO oxidation and N_2O + CO reaction. For activity evaluation, 0.1 g of each sample was placed between two quartz wool plugs (bed length ~1 mm), the reactant ($CO:O_2$:He = 2:1:17 for CO oxidation and $CO:N_2O$:He = 2:2:16 for CO + N_2O reaction) flow rate being at 40 ml min^{-1}. Volume reduction glass rods were inserted on both sides of the quartz wool plugs. Effluents were sampled and analyzed on a gas chromatograph (Porapak-Q column and thermal conductivity detector). The temperature dependent catalytic activity of all $La_2Ti_{2(1-x)}Fe_{2x}O_{7-\delta}$ samples was evaluated under continuous flow of reactant mixtures in range of 50–600 °C, by holding 1 h at each temperature. Each sample was initially pretreated at 350 °C for 2 h under N_2 flow prior to activity measurements. The catalytic conversions were calculated on the basis of product yield CO_2 for 0.1 g of each sample. The void volume fraction estimated for LTOGC and LF(0.4)GC were found to be 0.80, and 0.89, respectively.

3. Results and discussion

3.1. Phase characterization by XRD

Table 1 lists the abbreviations and phases identified from XRD patterns of all the nominal compositions $La_2Ti_{2(1-x)}Fe_{2x}O_{7-\delta}$ ($0.0 \le x \le 1.0$) prepared by two different routes viz. solid state and gel combustion. Henceforth in the present communication, all the samples will be referred by their abbreviation as mentioned in Table 1. The crystal growth of the lanthanum titanate, layered perovskite, $La_2Ti_2O_7$ phase as a function of calcination temperature was monitored by recording XRD diffraction pattern after calcinations at different temperatures. As the calcination temperature increased to 1200 °C the intensity of the unreacted phases due to TiO_2 and $La(OH)_3$ decreased, and the counts due to $La_2Ti_2O_7$ phase increased. The extra lines which were seen in XRD pattern of $La_2Ti_2O_7$ calcined at 900 °C appeared at 2θ = 25.2°, 28.2°, 29.2°, and 39.6°. These extra lines are attributed to the presence of free reactants in the sample corresponding to $La(OH)_3$ (JC-PDS card no. 36-1481) and TiO_2 (Brookite, JC-PDS card no. 29-1360). Also shift in d value by 0.055 in most intense reflection from $h\,k\,l$ of 2 1 2 planes at d value of 2.995 of parent phase is observed. These observations suggested that the solid state reaction is incomplete even at 1200 °C. For completion of diffusion controlled solid state reaction, all samples were further calcined at higher temperatures. The solid state reaction of La_2O_3 + TiO_2, and henceforth single phase synthesis of lanthanum titanate was observed at 1400 °C which crystallized in $A^{III}{}_2B^{IV}{}_2O_7$ lattice type having layered perovskite structure. The XRD patterns of samples ($0.0 \le x \le 1.0$) synthesized by solid state reaction calcined at 1400 °C are shown in Fig. 1(a–g). For modifying the powder/morphological properties of crystalline $La_2Ti_{2(1-x)}Fe_{2x}O_{7-\delta}$ samples, an alternative preparation route, gel combustion using citric acid as fuel was adopted. For comparison, the XRD patterns of corresponding samples synthesized by gel combustion are shown in Fig. 1(h–n). The XRD pattern of sample with x = 0.0 as shown in curve a of Fig. 1 matches with monoclinic $La_2Ti_2O_7$ (JC-PDS card no. 28-0517) having cell parameters as a = 13.015 Å, b = 5.5456 Å and c = 7.817 Å, z = 4, cell volume = 557.8 $Å^3$. However by gel combustion route the single $La_2Ti_2O_7$ phase was obtained when calcined at 800 °C as shown in curve h in contrast to 1400 °C (Fig. 1a) by solid state route. The crystal structure was also highly dependent on the doping content of Fe. As expected the substitution of lower valent Fe^{3+} in place of Ti^{4+} will decrease the extra oxygen in the $La_2Ti_2O_7$ phase. This is reflected in the change of layered perovskite to perovskite phase for the solid state samples having Fe more than 60% substitution. The samples having $x \ge 0.6$ (Fig. 1e–g) crystallizes in rhombohedral $LaFeO_3$ phase having unit cell parameters a = 5.566 Å, b = 7.854 Å, and c = 5.56 Å, Vol. = 242.81 $Å^3$ (JC-PDS card no. 37-1493). The crystallization of $LaFeO_3$ phase was induced even by meagre amounts of Fe doping as suggested by the presence of weak XRD line at 2θ = 32.19° marked as * in LF(0.1)SS/GC sample as shown by curve b of Fig. 1. The intensity of this line increased with increase in Fe content as seen in curves b–g and i–n in Fig. 1. At the same time the intensity of reflection due to 2 1 2 plane (100% line marked as #) in pyrochlore phase was found to diminish with increase in Fe content. As seen in curve d of Fig. 1 the intensity of XRD

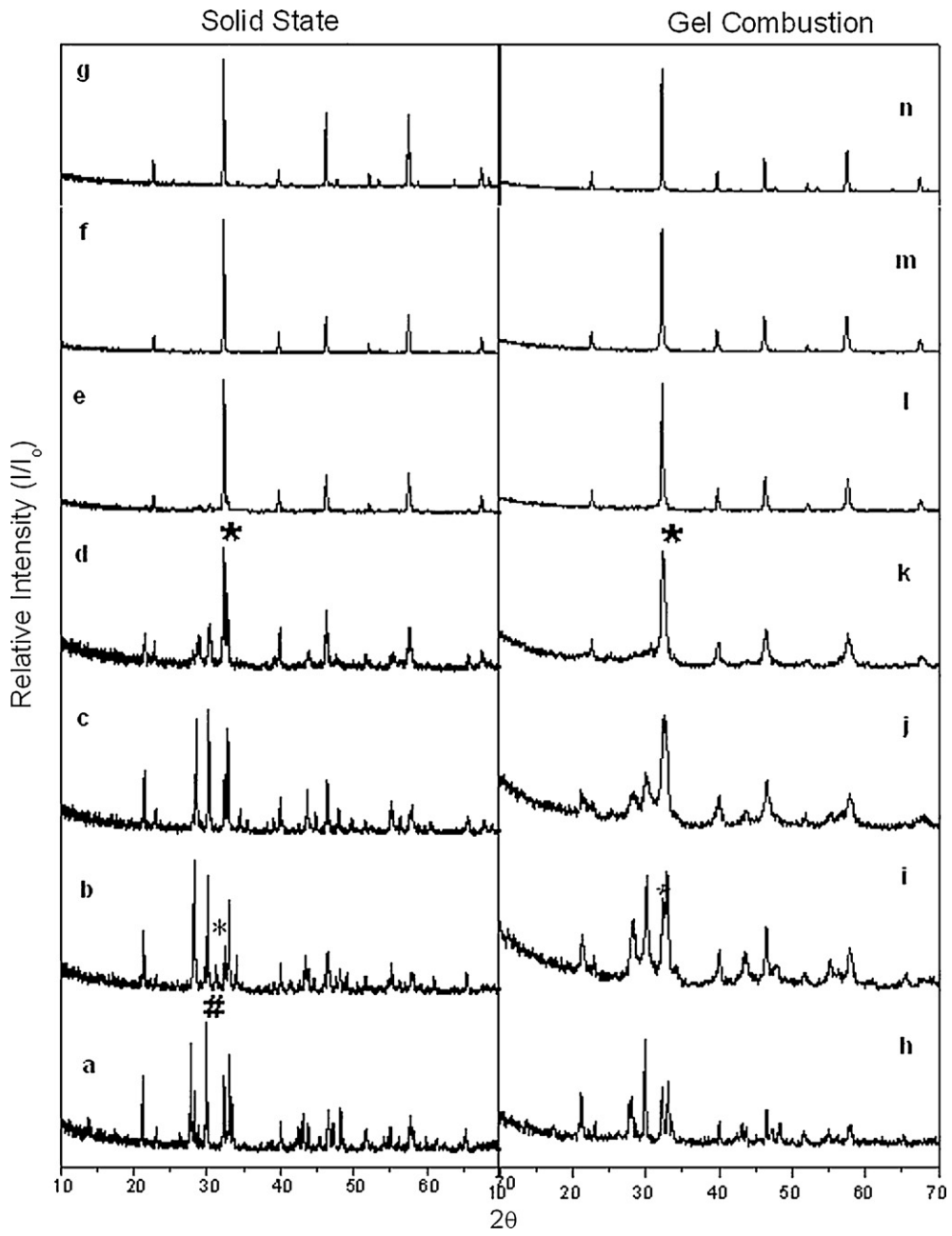

Fig. 1. XRD patterns of nominal compositions $La_2Ti_{2(1-x)}Fe_{2x}O_{7-\delta}$ synthesized by solid state (SS) reaction (a–g) and gel combustion (GC) route (h–n) for different samples, LTO (a, h), LF(0.1) (b, i), LF(0.2) (c, j), LF(0.4) (d, k), LF(0.6) (e, l), LF(0.8) (f, m), LFO (g, n). *XRD peak at $2\theta = 32.17$ attributed to perovskite $LaFeO_3$; #XRD peak at $2\theta = 29.8$ corresponds to $La_2Ti_2O_7$ phase.

line due to parent phase was drastically reduced to ~30.4% from 100% in LF(0.4)SS was absent in LF(0.8)SS and LFOSS (Fig. 1f and g). Thus Fe doping by solid state reaction stabilized the lanthanum titanate in perovskite lattice above 60% of substitution by lowering down the excess oxygen of the system. The single phased compositions in $La_2Ti_{2(1-x)}Fe_{2x}O_{7-\delta}$ ($A_2B_2O_7$) where $x \geq 0.6$ may be better represented as $2LaTi_{1-x}Fe_xO_{3+\delta}$ (ABO_3) perovskites. For instance, $La_2Ti_{0.8}Fe_{1.2}O_{7-\delta}$, can be represented by $2La(Ti_{0.4}Fe_{0.6})O_{3+\delta}$, oxide. The XRD patterns of samples synthesized by gel combustion route also revealed nearly same crystal structures as by ceramic route with some differences. Firstly, the XRD lines in curves i–k are very broad suggesting decrease in crystallite size of samples synthesized by gel combustion route (Table 1). Homogeneous mixture of reactants in gel combustion helped in achieving single phase, LF(0.4)GC sample whereas that synthesized by solid state route is biphasic with a mix of both the extreme phases. Also the unsubstituted LTO single phase was obtained at much lower temperature (800 °C) as compared to solid state reaction (1400 °C).

3.2. Crystallite size, surface area and pore size distribution

The increasing order of crystallite size as was calculated using Scherrer's equation observed from Table 2 is LF(0.4) ≈ LF(0.2) < LF(0.6) ≈ LF(0.8) < LTO < LFO. The cationic substitution of Fe^{3+} in $La_2Ti_2O_7$ lattice was accompanied with drastic decrease in crystallite size and formation of pores. Nanosized powders have been obtained by gel combustion route as compared to bulk oxides synthesized by solid state reaction (Table 2). For example LF(0.4)GC has a crystallite size of 14–17 nm as compared to 38–40 nm size of its solid state analogue LF(0.4)SS. It is interest-

Table 2
Crystallite size and N_2-BET surface area of nominal compositions $La_2Ti_{2(1-x)}Fe_{2x}O_{7-\delta}$ as calculated from XRD line width using Scherrer's equation.

S. no.	Value of x	Sample	Crystallite size (nm)		Surface area ($m^2\ g^{-1}$)	Pore size (Å)
			Gel combustion	Solid state calcined at 1400 °C	Gel combustion	
1	0.0	LTO	60–62	82–84	12	~400
2	0.2	LF(0.2)	14–16	51–53	14	~300
3	0.4	LF(0.4)	15–17	38–40	68	~20
4	0.6	LF(0.6)	40–42	50–52	47	~20
5	0.8	LF(0.8)	44–46	151–153	9	
6	1.0	LFO	77–80	100–102	7	

ing to note that both the solid state reaction and citrate complex decomposition route has led to same trend in crystallite size and surface area. The surface area of LF(0.4)GC and LF(0.6)GC calcined at 800 °C was found to be 68 and 47 $m^2\ g^{-1}$, respectively, considerably higher than unsubstituted LTOGC as well as LFOGC samples, with 12 and 7 $m^2\ g^{-1}$, respectively. Enhanced surface area of LF(0.6)GC (47 $m^2\ g^{-1}$) sample as compared to LF(0.2)GC of 14 $m^2\ g^{-1}$ is not in agreement with the trend followed by their crystallite size (Table 2). This anomaly in trends can be explained from their pore size distribution curves (Fig. 2) where LF(0.6)GC sample have maximum pores of radii ~20–30 Å exists, whereas larger pores with radii >200 Å are observed in LF(0.2)GC sample. Citrate nitrate gel combustion method has previously yielded porous powders with high surface areas [24,25]. However, further addition of Fe^{3+} in Ti^{4+} site has resulted in increase in the particle size as can be seen in Table 2 for LF(0.8)GC and LFOGC samples which are having crystallite size of the order of 40–42 and 77–80 nm, respectively. This, suggest that the substitution-induced microstructural defects and nonstoichiometry created on lattice reorganization during synthesis also play a role in deciding the morphology of the sample. This result is well in agreement with our earlier studies, where Fe substitution at B-site cation in $La_{0.8}Sr_{0.2}MnO_{3-\delta}$ lattice (LSM)

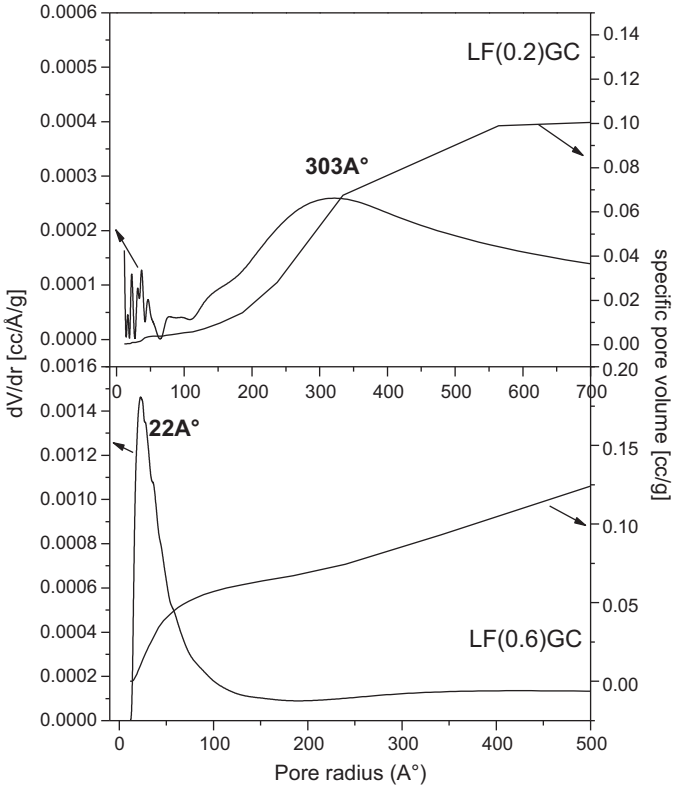

Fig. 2. BJH pore size distribution and cumulative volume curves of LF(0.2)GC and LF(0.6)GC samples.

[22] and in In_2TiO_5 [18] has played a significant role to decrease the crystallite size of $La_{0.8}Sr_{0.2}Mn_{1-x}Fe_xO_{3-\delta}$ (LSMF) and indium titanate samples, respectively. Similar results have been obtained by other researchers, for instance, Taguchi et al. [26] have demonstrated that the crystallite size decreased with increasing x in the perovskite-type $(La_{1-x}Ca_x)FeO_3$ samples and such samples with smaller particle size exhibited a higher catalytic activity.

3.3. Scanning electron microscopy

Fig. 3a–c shows the microstructures of the LTOGC, LF(0.2)GC, LF(0.4)GC pellets synthesized by gel combustion method. The micrograph of LTOGC (Fig. 3a) reveals the presence of elongated rod like structures. While, 40–60% Fe substitution resulted in more or less spherical shaped geometry as observed in the SEM micrograph of LF(0.4)GC (Fig. 3c). The inhibition of grain size observed as a result of Fe substitution may be due to the creation of defects in the doped samples. The LTOGC and LF(0.4)GC crystallizes in layered perovskite structure and latter sample is ideal perovskite as confirmed by their XRD patterns. The rod like structures forming layers can be attributed to the layered perovskite, $La_2Ti_2O_7$ phase present on the surface of LTOGC sample (Fig. 3a) whereas spherical grains are due to perovskite, ABO_3 arrangement of cations and anions in LF(0.4)GC (Fig. 3c). The mixed phases are observed in case of LF(0.2)GC as observed in its SEM image (Fig. 3b) where both rod like and spherical grains are present. The crystallite sizes reported in Table 2 are calculated from the FWHM of the 100% peak in the XRD pattern of the sample which gives us the average crystallite size using Scherrer's equation. While in SEM, we have reported the microstructure of the sample pellets revealing their grain size. So it is the grain size which is reflected in the SEM.

3.4. FTIR

Infrared spectroscopy can be used to monitor chemical and structural changes in the mixed metal oxides. The FTIR spectra of all the prepared solid state oxides in KBr are shown in Fig. 4. Table 3 shows the characteristic IR bands (cm^{-1}) and their assignments observed in FTIR spectra recorded for various samples. A prominent absorption band at 552 cm^{-1}, a broad band at 618 cm^{-1}, several weak bands between 400 and 500 cm^{-1} in addition to three bands above 700 cm^{-1} are observed in the FTIR spectrum (Fig. 4a) of pristine lanthanum titanate, LTOSS. The vibration bands for absorption bands of TiO_6 octahedra are generally lower than 700 cm^{-1}. The bands below 405 cm^{-1} are assigned to Ti–O bending vibration and those above 405 cm^{-1} are attributed to Ti–O stretching vibration [27–29]. On the other hand, rare earth oxygen stretching modes generally lie in the region of 300–500 cm^{-1}. Thus, the bands in the 400–500 cm^{-1} region in LTOSS can be attributed to complex motions involving the participation of both La and Ti cations [30]. The strong peak at 550 cm^{-1} can be assigned to Ti–O vibration in TiO_6 octahedra present in the structure. There are two additional bands at 750 cm^{-1} and 805 cm^{-1} which are of higher frequencies generally observed in M_2TiO_5 compounds at about 775 cm^{-1} due

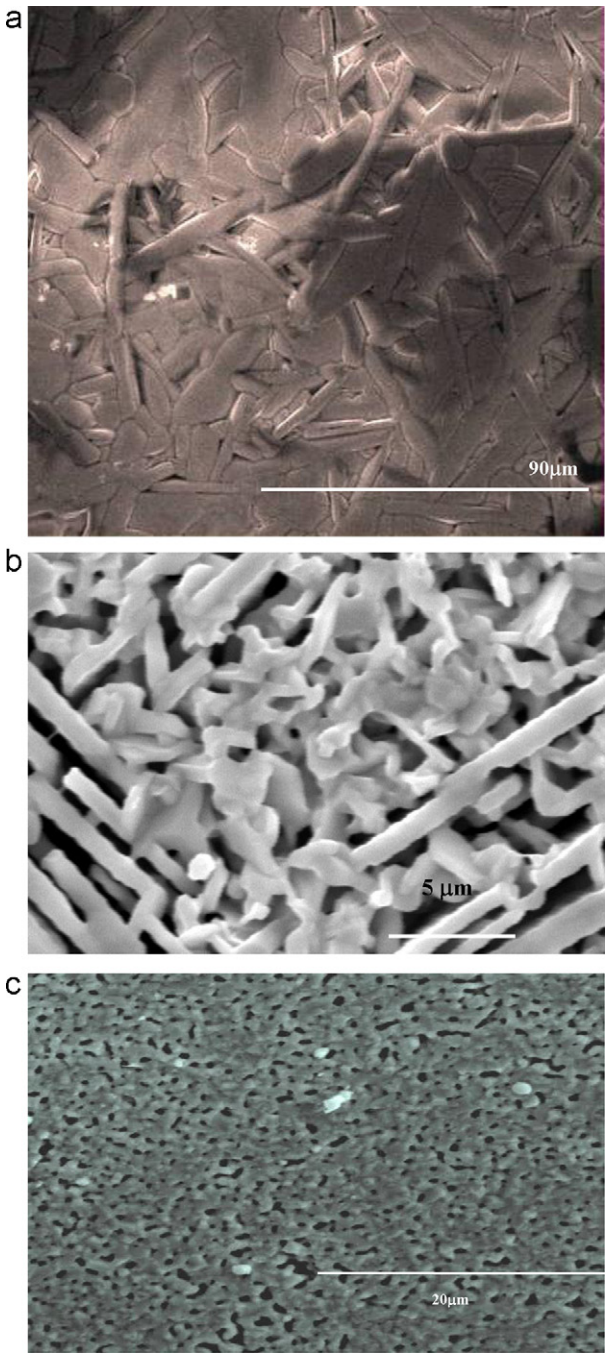

Fig. 3. Scanning electron micrographs of (A) LTOGC, (B) LF(0.2)GC and (C) LF(0.4)GC samples.

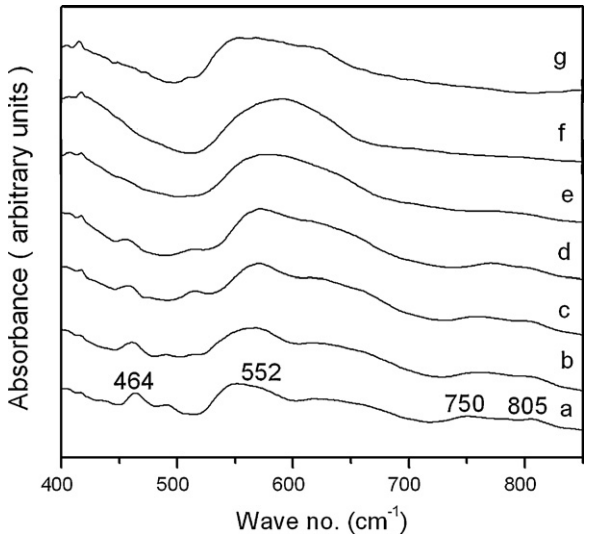

Fig. 4. FTIR spectra of nominal compositions $La_2Ti_{2(1-x)}Fe_{2x}O_{7-\delta}$ as a function of Fe content. (a) LTO, (b) LF(0.1)SS, (c) LF(0.2)SS, (d) LF(0.4)SS, (e) LF(0.6)SS, (f) LF(0.8)SS, and (g) LFOSS.

to one short Ti–O bond in TiO_5 groups present in such compounds [31] and also in tetrahedrally coordinated TiO_4 units, as smaller the coordination number, the shorter the bond length and higher the vibrational frequencies [32]. No such possibilities arise in LTOSS as the lattice consists of slabs of corner sharing TiO_6 octahedra. Therefore, vibrational bands observed at higher wave numbers in LTOSS can be assigned to Ti–O stretching where the oxygen ion is shared between two octahedrally coordinated titanium ion and two nine-fold coordinated lanthanum ion.

As we substitute Fe at Ti site in LTOSS the higher vibrational bands (>700 cm^{-1}) gradually weakens (Fig. 4b–g) and ultimately disappears in LF(0.8)SS which further confirms the XRD observations corresponding to the transformation from layered perovskite to perovskite lattice. Besides, due to the combined effect of Ti–O stretching and Fe–O stretching the band at ~550 cm^{-1} broadens with increase in Fe content (Fig. 4b–g). The peak at ~ 416 cm^{-1} sharpens with increase in Fe substitution because of the presence of O–Fe–O deformation vibration as observed in curves b–g of Fig. 4. The other extreme LFOSS (Fig. 4g) shows two bands, one at 415 cm^{-1} which can be attributed to Fe–O–Fe deformation vibration and another very prominent and broad band at 567 cm^{-1} which can be assigned to Fe–O stretching vibration [33].

3.5. Mössbauer spectroscopy

Fig. 5 presents room temperature Mössbauer spectra of nominal compositions $La_2Ti_{2(1-x)}Fe_{2x}O_{7-\delta}$ typically for values of $x = 0.1$, 0.4 and 0.8 prepared by solid state (Fig. 5a–c) and gel combustion route (Fig. 5d–g). The corresponding values of Mössbauer parameters:

Table 3
Position and assignments of the observed vibrational bands for nominal compositions $La_2Ti_{2(1-x)}Fe_{2x}O_{7-\delta}$ with different values of x.

S. no.	x	Sample	Vibrations (cm^{-1}) and their assignments						
			Complex vibrations involving both La and Ti/δ_{FeOFe} [29]			ν_{TiO}/ν_{FeO}		ν_{TiO} [30]	ν_{TiO} [31]
1	0.0	LTOSS	417	464	490w	552vs	618sh,b	750s	805s
2	0.1	LF(0.1)SS	415	464	490	568	616sh	762	807
3	0.2	LF(0.2)SS	416	458	475sh	570vs	620sh	760w	804w
4	0.4	LF(0.4)SS	416	456		571vs	615sh	770w	800w
5	0.6	LF(0.6)SS	416	450w		575vs			
6	0.8	LF(0.8)SS	417			590vs,b			
7	1.0	LFOSS	415 [32]	450w	474w	567vs,b [32]			

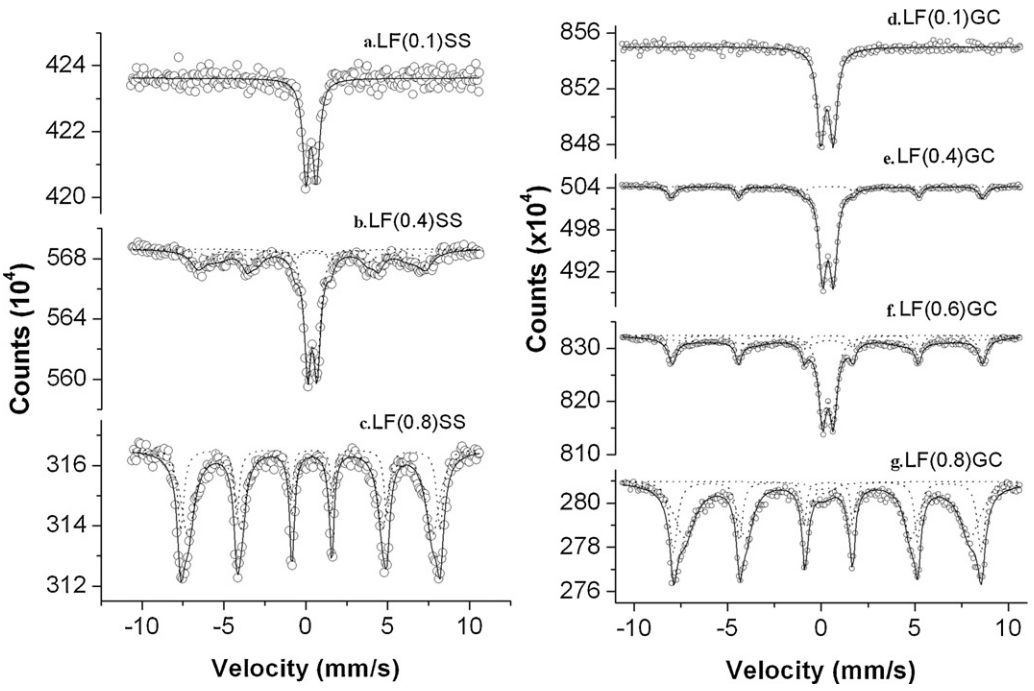

Fig. 5. Mössbauer spectra of nominal compositions $La_2Ti_{2(1-x)}Fe_{2x}O_{7-\delta}$ {LF(x)} synthesized by (a–c) solid state route and (d–g) gel combustion route. Component spectra are shown by dotted lines. (a) LF(0.1)SS, (b) LF(0.4)SS, (c) LF(0.8)SS, (d) LF(0.1)GC, (e) LF(0.4)GC, (f) LF(0.6)GC, and (g) LF(0.8)GC.

magnetic hyperfine values (H_{hf}), isomer shift (δ), quadrupole splitting (ΔE_Q), and area in percentage of tetrahedral and octahedral sites of Fe^{3+} ions at room temperature for $La_2Ti_{2-x}Fe_xO_{7-\delta}$ samples synthesized by both these routes gel combustion and solid state are listed in Tables 4 and 5. Mössbauer spectra reveal that Fe is present in trivalent state in all the substituted samples but its coordinative environment depended upon Fe content. Mössbauer spectrum of LF(0.1)SS could be fitted into one symmetric paramagnetic doublet, with a large quadrupole splitting (ΔE_Q):0.643 mm/s and isomer shift (δ) of ~0.358 mm/s, line width (Γ):0.474 mm/s (Fig. 5a) as mentioned in Table 4. This paramagnetic doublet is attributed to the presence of Fe^{3+} ions in an octahedral oxygen lattice distributed homogeneously in the sample [34]. With increasing iron content in samples LF(0.4)SS and LF(0.8)SS a gradual transition from paramagnetic to magnetic (ferro- or antiferro-) can be noted. This is reflected clearly in the presence of two hyperfine-split sextets in LF(0.4)SS and LF(0.8)SS as shown in curves b and c, respectively, of Fig. 5. The isomer shift for these sextets varies

Table 4
Mössbauer parameters: magnetic hyperfine values (H_{hf}), isomer shift (δ), quadrupole splitting (ΔE_Q), and area in percentage of tetrahedral and octahedral sites of Fe^{3+} ions at room temperature for nominal compositions $La_2Ti_{2(1-x)}Fe_{2x}O_{7-\delta}$ synthesized by solid state reaction.

$La_2Ti_{2(1-x)}Fe_{2x}O_{7-\delta}$ (SS)	Sample	Iron sites	Isomer shift (δ)	Quadrupole splitting (ΔE_Q) (mm/s)	Hyperfine values (H_{hf}) (kG)	Width (Γ) (mm/s)	Area (%)
$x = 0.1$	LF(0.1)SS	Doublet	0.358	0.643	–	0.474	100
$x = 0.4$	LF(0.4)SS	Doublet	0.380	0.575	–	0.495	44.1
		Sextet 1	0.403	0.029	432.3	1.031	24.9
		Sextet 2	0.330	0.002	371.1	1.938	31.0
$x = 0.8$	LF(0.8)SS	Sextet 1	0.378	0.043	492.6	0.478	31.1
		Sextet 2	0.356	0.041	464.9	1.020	68.9

Table 5
The magnetic hyperfine values (H_{hf}), isomer shift (δ), quadrupole splitting (ΔE_Q), and area in percentage of tetrahedral and octahedral sites of Fe^{3+} ions at room temperature for nominal compositions $La_2Ti_{2(1-x)}Fe_{2x}O_{7-\delta}$ synthesized by gel combustion route.

$La_2Ti_{2(1-x)}Fe_{2x}O_{7-\delta}$ GC	Sample	Iron sites	Isomer shift (δ)	Quadrupole splitting (ΔE_Q) (mm/s)	Hyperfine field (H_{hf}) (kG)	Width (Γ) (mm/s)	Area (%)
$x = 0.1$	LF(0.1)GC	Doublet	0.313	0.677	–	0.474	100
$x = 0.4$	LF(0.4)GC	Doublet	0.364	0.579	–	0.479	79.65
		Sextet 1	0.468	0.414	516.6	0.512	20.35
$x = 0.6$	LF(0.6)GC	Doublet	0.360	0.571	–	0.497	34.19
		Sextet 1	0.395	0.032	515.3	0.512	22.24
		Sextet 2	0.416	0.090	429.7	1.211	43.57
$x = 0.8$	LF(0.8)GC	Doublet	0.193	0.001	–	1.237	03.31
		Sextet 1	0.399	0.033	510.7	0.532	30.61
		Sextet 2	0.383	0.029	474.2	1.211	66.08

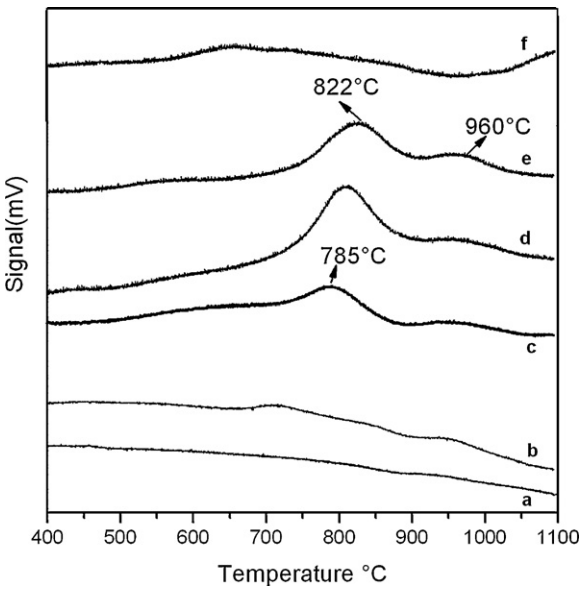

Fig. 6. TPR cycles of nominal compositions $La_2Ti_{2(1-x)}Fe_{2x}O_{7-\delta}$ synthesized by solid state route. (a) LTOSS, (b) LF(0.2)SS, (c) LF(0.4)SS, (d) LF(0.6)SS, (e) LF(0.8)SS, and (f) LFOSS.

between 0.3 and 0.4, the quadrupole splitting and values of other Mössbauer parameters as mentioned in Table 4. These sextets may be ascribed to Fe^{3+} cations located at distorted octahedral sites, thus suggesting the existence of domains/regions with varying local fields. This distortion in symmetry in LF(0.4)SS sample may arise due to anisotropic deformation of the environment of the Fe^{3+} ions due to oxygen vacancies generated by substitution at Ti^{4+} sites. The sample LF(0.8)SS exhibits only two magnetic sextets (Fig. 5c) with hyperfine magnetic field (H_{hf}) values are 492.6 kG (octahedral sites) and 464.9 kG (tetrahedral sites), revealing the relative concentration of Fe in octahedral and tetrahedral sites, respectively, as shown in Table 4. These results thus reveal the presence of iron in at least two distinct environments, the relative abundance of which may depend upon Fe-content. The Mössbauer spectroscopy results also show that the hyperfine field (H_{hf}) increased progressively, as one goes to LF(0.8)SS (Fig. 5c) from LF(0.4)SS (Fig. 5b), indicating that Fe is more magnetically ordered in LF(0.8)SS. This is further supported by the lower ΔE_Q (quadrapole splitting) values for LF(0.8)SS samples as compared to LF(0.4)SS as seen from Table 4.

Similarly corresponding spectra recorded for samples prepared by gel combustion route are shown in Fig. 5d–g, reveals that intensity of the magnetic component increases with the increase in Fe substitution. 60–80% Fe substituted samples prepared by gel combustion shows the existence of Fe in three distinct environments which is evident by presence of one paramagnetic doublet and two magnetic sextets as shown in Fig. 5f and g. The large quadrupole splitting (ΔE_Q) as observed from Table 5 for gel combustion samples is characteristic of very small crystallites (nanocrystalline nature), their large surface to volume ratio causing large lattice strain and a correspondingly large electric field gradient at the iron nuclei [35].

3.6. Temperature programmed reduction (TPR)

The TPR profiles of nominal compositions $La_2Ti_{2(1-x)}Fe_{2x}O_{7-\delta}$ ($0.0 \le x \le 1.0$) are presented in Fig. 6. Pristine LTOSS sample shows a weak reduction profile with minimal reduction (Fig. 6a). Substitution by reducible cation, Fe^{3+} in place of Ti^{4+} enhanced reducibility in temperature range of 700–800 °C as shown in curves b–f of Fig. 6. The area under the peak corresponds to quantitative estimation of H_2 consumed for the reduction of $Fe^{3+} \rightarrow Fe^0$ in the substituted samples. The amount of H_2 consumption increases with increase in Fe content in substituted samples. Partial Fe substitution helped in facilitating completion of reduction cycle below 1000 °C, which was extended beyond 1100 °C in parent samples, LTOSS and LFOSS (Fig. 6a and f). Poor reducibility of LTOSS is in agreement with the observation commonly seen in scheelites and pyrochlore structures, oxygen rich compositions in which diffusivity of oxygen is restricted. The changes in the TPR profiles as a result of Fe substitution can be ascribed to the nonstoichiometry and imperfections generated in the single phased compositions. The decrease in T_{max} in LF(0.4)SS sample is attributed to greater non-stoichiometry caused by substitution of an aliovalent cation at B site facilitating the lattice oxygen diffusion via anionic vacancies generated in the process. The reduction behavior of the samples having single $LaFeO_3$ phase thus show reduction behavior of metal–oxygen bond typically as that in perovskites. In these structures, oxygen overstoichiometry is accommodated within the perovskite framework in randomly distributed short range linear defects as recently reported [1,7]. The two peak pattern observed at ~820 °C and ~960 °C in TPR profile of LF(0.8)SS (Fig. 6e) is in accordance with its Mössbauer spectra (Fig. 5c) where existence of Fe in two distinct sites, i.e., octahedral and tetrahedral is revealed. Reduction of Fe in octahedral sites occurs at lower temperature than tetrahedral sites as bulk oxygen from Fe–O bond in FeO_6 coordination is labile as compared to desorptivity of oxygen from Fe–O bond in FeO_4 coordination. The T_{max} of the individual peaks in LF(0.4)SS (Fig. 6c), was found to be at ~785 °C as compared to ~822 °C in sample having 80% Fe substitution, i.e. LF(0.8)SS (Fig. 6e). The increase in T_{max} from LF(0.4)SS to LF(0.8)SS and LFOSS indicates that lesser number of the defects is created in the sample as the ideal perovskite is reached in samples having Fe content higher than 80%. The mobility of lattice oxygen is restricted in the ideal perovskite as compared to disordered lattice as evident by Mössbauer results and therefore increase in T_{max} is observed for LF(0.8)SS and LFOSS samples as compared to disordered LF(0.4)SS perovskite.

The effect of modified surface properties of powder oxides and higher surface area on the reduction behavior is shown in Fig. 7. Typical first TPR cycle of LF(0.4)GC and LF(0.4)SS sample is shown in Fig. 7. LF(0.4)GC sample synthesized by gel combustion route shows a reduction peak at 510 °C in addition to main reduction band at ~800 °C as seen in Fig. 7. The higher surface area (68 $m^2\,g^{-1}$), and decreased particle size (14–17 nm) of sample as mentioned in Table 2, synthesized by gel combustion route induces ease in diffusivity and reactivity of hydrogen lowering the activation barrier, induces ease in reducibility of sample at lower temperature.

3.7. Phase identification of reduced samples

The XRD patterns of TPR residue of LTOSS and Fe substituted LF(0.8)SS samples after reduction are compared with the fresh samples in Fig. 8. The reduction in 5% H_2/Ar did not affect the XRD of these samples significantly as evident from Fig. 8. Thus the oxygen excess titanate LTOSS show considerable structural and phase stability even after reduction. Since there is no significant change in lattice after reduction for LF(0.8)SS, it gives an indication that along with Fe^{3+}, Ti^{4+} is also undergoing reduction and converts to metallic Fe and Ti^{3+}. This indicates that hydrogen swipes away the extra oxygen from the system and stabilizes the reduced species Ti^{3+} in the ABO_3 type of lattice. The considerable phase stability of LTOGC on reduction makes it a preferred prospective support [36] for dispersion of metal ions where it can show excellent oxygen storage capacity.

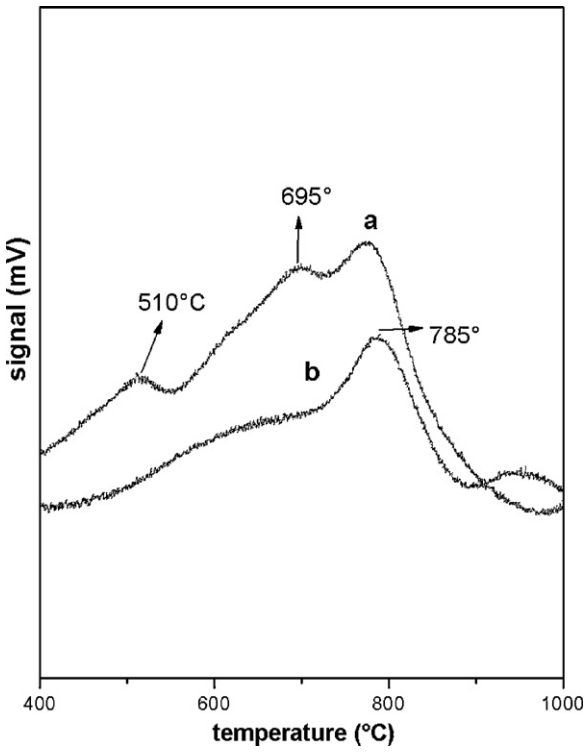

Fig. 7. Effect of synthetic route on reduction behavior of the sample is shown by comparing first TPR profile of LF(0.4)GC (a) and LF(0.4)SS (b) prepared by gel combustion and solid state route, respectively.

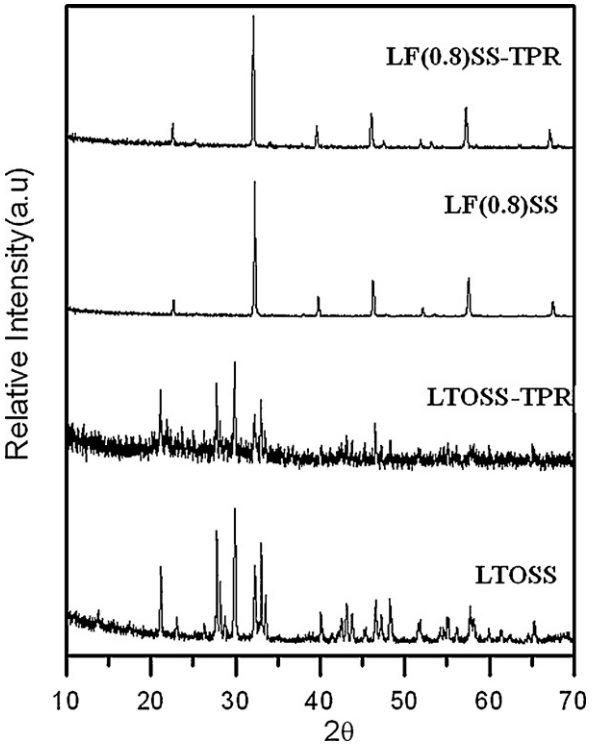

Fig. 8. XRD patterns of unsubstituted $La_2Ti_2O_7$ (LTOSS) and Fe substituted $La_2Ti_{0.4}Fe_{1.6}O_{7-\delta}$ {LF(0.8)SS} samples before and after First TPR cycle.

3.8. Catalytic activity

3.8.1. $CO + N_2O$ reaction

The temperature dependent catalytic activity of nominal compositions $La_2Ti_{2(1-x)}Fe_{2x}O_{3+\delta}$ synthesized by solid state route (a–g) and gel combustion (h–m) for decomposition of N_2O using CO viz.; $CO + N_2O$ reaction is exhibited in Fig. 9. The reactant mixture of $CO:N_2O:He = 2:2:16$ was fed to the catalyst at a rate of 40 ml/min. Partially Fe substituted samples have shown better activity as compared to unsubstituted samples. Unsubstituted samples, $La_2Ti_2O_7$ (LTOSS) and $LaFeO_3$ (LFOSS) have shown poor activity of ~80% and 100% at 700 °C as shown in Fig. 9a and b, respectively. LF(0.1)SS and LF(0.2)SS (curves c and d) samples have shown slightly better activity than unsubstituted LTOSS but similar to LFOSS phase. Whereas LF(0.4)SS sample resulted in considerable rise in activity as shown in curve e with 80% conversion at 450 °C in contrast to mere 10% and 35% conversion by unsubstituted samples. Maximum conversion of 100% was observed over the LF(0.4)SS sample at 550 °C for $CO + N_2O \rightarrow CO_2 + N_2$ reaction (Fig. 9e). The light off temperature for LF(0.4)SS sample was at ~275 °C much lower as compared to ~400 °C in case of unsubstituted sample LTOSS. LF(0.6)SS and LF(0.8)SS with higher Fe content have considerably activity (Fig. 9f and g) but lower than LF(0.4)SS sample. The decreasing order of activity LF(0.4)SS > LF(0.6)SS > LF(0.8)SS > LF(0.2)SS > LFOSS > LF(0.1)SS > LTOSS was observed in solid state samples.

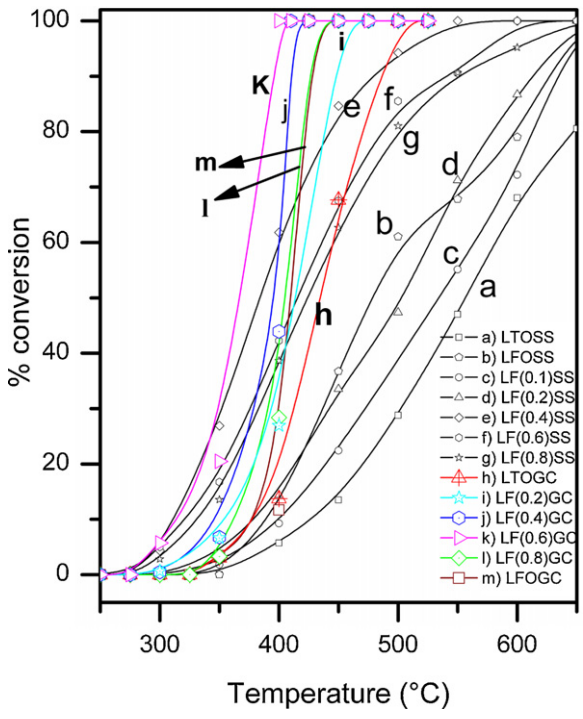

Fig. 9. The temperature dependent activity of nominal compositions $La_2Ti_{2(1-x)}Fe_{2x}O_{7-\delta}$ synthesized by solid state (a–g) and gel combustion route (h–m) for $CO + N_2O$ reaction.

Gel combustion synthesis has imparted enhanced catalytic activity to these $La_2Ti_{2(1-x)}Fe_{2x}O_{3+\delta}$ samples as compared to their solid state analogues (Fig. 9h–m). Catalytic activities of unsubstituted LTOGC and LFOGC with single phase $La_2Ti_2O_7$ and $LaFeO_3$ phases, respectively, have shown mere ~20% and ~45% conversion at 400 °C, respectively, in curves h and m of Fig. 9. Thus, pure single phase are not responsible for high activity. LF(0.2)GC and LF(0.8)GC (curves i and m) samples have shown 100% conversion at ~450 °C. LF(0.4)GC sample resulted in considerable rise in activity as shown in curve j with 100% conversion at 425 °C in comparison to other samples. Among all samples, maximum conversion of 100% occurred over LF(0.6)GC at ~395 °C as shown in Fig. 9k for $CO + N_2O \rightarrow CO_2 + N_2$ reaction. The catalytic activity for $CO + N_2O$ reaction on gel combustion synthesized samples follows, LF(0.6)GC > LF(0.4)GC > LF(0.8)GC ≈ LFOGC > LF(0.2)GC > LTOGC a

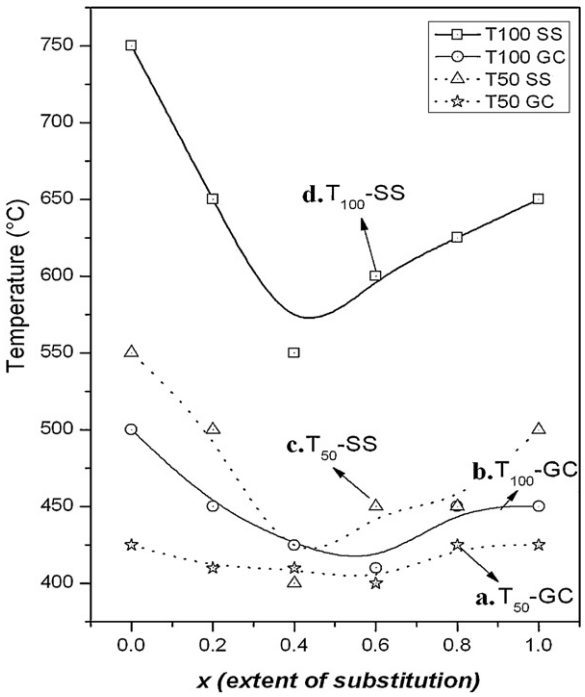

Fig. 10. Effect of Fe substitution on T_{50} (a, c)and T_{100} (b, d), temperatures at which 50% and 100% conversions were obtained over nominal compositions $La_2Ti_{2(1-x)}Fe_{2x}O_{7-\delta}$ synthesized by gel combustion (a, b) and solid state (c, d) routes for $CO + N_2O$ reaction.

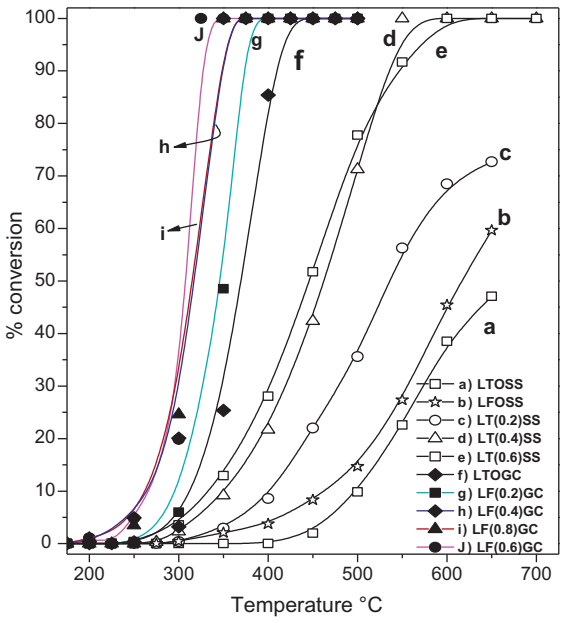

Fig. 11. Temperature dependent catalytic activity of nominal compositions $La_2Ti_{2(1-x)}Fe_{2x}O_{7-\delta}$ samples synthesized by solid state and gel combustion routes for $CO + O_2$ reaction.

trend similar as above for solid state samples at lower activity level with an exception for the most active sample (Fig. 9).

Plot of T_{50} and T_{100} values vs. x (extent of substitution) in nominal compositions $La_2Ti_{2(1-x)}Fe_{2x}O_{3+\delta}$ is shown in Fig. 10. T_{50} and T_{100} suggests the temperatures at which 50% and 100% conversion for $CO + N_2O$ reaction achieved in all substituted and unsubstituted samples synthesized by both the routes. Both T_{100} and T_{50} values are lowest for LF(0.4)SS and LF(0.6)GC suggesting that 40–60% Fe substitution leads to catalytically active compositions synthesized by either route for $CO + N_2O$ reaction. Gel combustion synthesis has improved activity in temperature range of 395–525 °C lower by ~150–225 °C than corresponding solid state samples (550–750 °C) although there is not much decrease in the onset of reaction as evident by curves b and d of Fig. 10. The difference in T_{50} and T_{100} values (curves a and b) of samples synthesized by GC route is ~28 °C much lower as compared to corresponding curves (c and d) of solid state synthesized samples (250 °C) in Fig. 10. Thus, after the onset of reaction, rate increases steeply with rise in temperature over fine powders of $La_2Ti_{2(1-x)}Fe_{2x}O_{3+\delta}$ synthesized by gel combustion, in contrast to sluggish rate observed in solid state analogues (Figs. 9 and 10).

3.8.2. CO oxidation

Nominal compositions $La_2Ti_{2(1-x)}Fe_{2x}O_{3+\delta}$ were also evaluated for CO oxidation reaction to support and establish the structure–activity correlations. In this case, the reactant mixture comprising of $CO:O_2:He = 2:1:17$ was fed to the catalyst at a rate of 40 ml/min. Fig. 11 presents the temperature dependent catalytic activity of $La_2Ti_{2(1-x)}Fe_{2x}O_{3+\delta}$ solid state (a–e) and combustion route (f–j) samples for $CO + O_2$ reaction. Samples prepared by softer route shifted the temperature window from 400–700 °C (Fig. 11a–e) to 200–400 °C (curves f–j). Gel combustion synthesis has induced activity in all Fe substituted samples even at 325 °C, whereas corresponding solid state samples do not show any conversion at 325 °C. Similar to $CO + N_2O$ reaction, partially Fe substituted samples have shown better activity as compared to both the unsubstituted phase LTOSS and LFOSS. Maximum conversion of 100% at ~325 °C with an onset at ~175 °C over LF(0.6)GC combustion route samples (Fig. 11j). Whereas among solid state samples maximum activity of 100% conversion at 550 °C, with the onset at 250 °C for CO_2 formation over LF(0.4)SS (curve d) was observed. All other samples, particularly unsubstituted phases, have shown reduced activity (Fig. 11). The decreasing order of activity for $CO + O_2$ reaction is LF(0.6)GC > LF(0.4)GC ≈ LF(0.8)GC > LF(0.2)GC > LTOGC for gel combustion and LF(0.4)SS > LF(0.6)SS > LF(0.2)SS > LFOSS > LTOSS for the solid state synthesized samples as revealed from Fig. 11.

3.8.3. Surface–bulk-activity correlations

The decreasing order of activity as revealed from Figs. 9–11 for $CO + N_2O$ as well as $CO + O_2$ reaction is: LF(0.4)SS > LF(0.6)SS > LF(0.2)SS > LFOSS > LTOSS in case of solid state prepared samples and LF(0.6)GC > LF(0.4)GC ≈ LF(0.8)GC > LF(0.2)GC > LTOGC for combustion samples. The activity order is similar for the samples synthesized by same route irrespective of the reaction. In both the reactions, CO oxidation occurs either by N_2O or by O_2, the maximum activity was obtained over LF(0.6)GC and LF(0.4)SS samples. Substituted samples with 40–60% Fe are most active catalytic formulations irrespective of the preparation route. However, 100% conversion for CO oxidation occurs at 325 °C as compared to 395 °C for $CO + N_2O$ reaction over LF(0.6)GC, the most active sample, suggesting that CO oxidation is the driving force for the reduction of N_2O by CO. The difference in activity can be attributed to presence of oxygen in CO oxidation which assists the oxidation reaction over LF(0.6)GC sample, also O_2 is stronger oxidizing agent as compared to N_2O. Whereas in $CO + N_2O$ reaction, CO is oxidized by facile lattice oxygen as suggested by catalytic activity results which is further confirmed by *in situ* FTIR studies presented elsewhere [9].

Catalytic activity of solid state samples calcined at 1400 °C with negligible surface area could be attributed only to crystal structure and modified bulk properties as a result of Fe substitution. Substitution by more reducible cation, i.e., Fe^{3+} at Ti^{4+}

sites resulted increased reducibility with decreased T_{max} observed in TPR profile of LF(0.4)SS. Studies investigated by Mössbauer spectroscopy also corroborate these results wherein asymmetry around the Fe^{3+} ions imparted by nonstoichiometry-induced anionic vacancies is clearly evident (Fig. 4d) and are responsible for maximum conversion of 100% at 550 °C observed over LF(0.4)SS. In case of samples prepared by gel combustion, surface area is greatly enhanced, particularly in LF(0.4)GC (~68 $m^2 g^{-1}$) and LF(0.6)GC (~47 $m^2 g^{-1}$), both are active but LF(0.6)GC shows maximum activity as against their surface area trend. This suggests that along with enhanced adsorption active sites on the surface, crystal structure also plays an important role in deciding their catalytic properties. Both LF(0.4)GC and LF(0.6)GC are single phased $LaFeO_3$ samples, where LF(0.6)GC sample is more crystalline. An increased crystallinity ensures easy diffusion path of lattice oxygen via anionic vacancies properly generated in nonstoichiometric LF(0.6)GC sample. The Mössbauer spectroscopy results also show that the hyperfine field (H_{hf}) increased progressively, as one goes to LF(0.8)SS (Fig. 5c) from LF(0.4)SS (Fig. 5b), indicating that Fe is more magnetically ordered in LF(0.8)SS. The increase in T_{max} from LF(0.6)SS to LFOSS sample (Fig. 6d and f, respectively) may be attributed to increase in symmetric ordering of Fe in case of higher substituted LF(0.8)SS sample, as evident by Mössbauer results (Fig. 3) resulting in decreased catalytic activity of single phased crystalline LF(0.8)SS and LFOSS samples as compared to LF(0.4)SS. Thus, enhanced catalytic activity of LF(0.6)GC is attributed to more active $LaFeO_3$ phase with increased surface area. While modified bulk properties, like maximum asymmetric distortion around Fe^{3+} atom, enhanced reducibility and substitution-induced anionic vacancies in nonstoichiometric LF(0.4)SS sample has maximized its activity for both the reactions.

4. Conclusion

Role of surface/bulk properties on catalyst performance was emphasized in the present study by applying both citrate combustion synthesis and conventional routes of synthesis. Here, replacement of Ti^{4+} by lower valence Fe^{3+} cation, created anionic vacancies that might favor lattice oxygen mobility and activity. Combustion route helped in achieving single phase, nanosized porous LF(0.4)GC and LF(0.6)GC samples at 800 °C in contrast to 1400 °C required for solid state synthesis. Fe substitution led to considerable rise in surface areas of order of ~68 $m^2 g^{-1}$ and ~47 $m^2 g^{-1}$ in LF(0.4)GC and LF(0.6)GC samples accompanied with formation of pores of 20–30 Å radius, as compared to unsubstituted, sample, LTOGC with poor surface area of ~12 $m^2 g^{-1}$. The increase in T_{max} from LF(0.6)SS to LFOSS (Fig. 6d and f, respectively) may be attributed to increase in symmetric ordering of Fe in case of higher substituted LF(0.8)SS, as evident by Mössbauer results (Fig. 4) also manifested in their lower catalytic activity. Among all samples, the maximum conversion of 100% occurred over LF(0.6)GC at ~395 °C for CO + N_2O and at ~325 °C for CO oxidation reaction. In conclusion we may state that enhanced catalytic activity of LF(0.6)GC is attributed to nonstoichiometric single $LaFeO_3$ phase with higher surface area. This suggests that along with enhanced adsorption active sites on the surface, crystal structure also plays an important role in deciding their catalytic properties. While modified bulk properties, like maximum asymmetric distortion around Fe^{3+} atom, enhanced reducibility and substitution induced-anionic vacancies in nonstoichiometric LF(0.4)SS sample has maximized its activity for both the reactions.

Reaction mechanism investigated by *in situ* FTIR studies by the authors over these samples for the decomposition of N_2O using CO is recently published elsewhere [9].

References

[1] J. Canales Vázquez, S.W. Tao, J.T.S. Irvine, Solid State Ionics 159 (2003) 159–165.
[2] W.F. Libby, Science 171 (1971) 499–500.
[3] M.M. Milanova, M. Kakihana, M. Arima, M. Yashima, M. Yoshimura, J. Alloys Compd. 242 (1996) 6–10.
[4] J. Happel, M.A. Hnatow, L. Bajars, M. Kundrath, Ind. Eng. Chem. Prod. Res. Dev. 14 (1975) 154–158.
[5] J.G. MacChesney, H.A. Sauer, J. Am. Ceram. Soc. 45 (1962) 416–422.
[6] D.W. Hwang, H.G. Kim, J.S. Lee, J. Kim, W. Li, S.H. Oh, J. Phys. Chem. B 109 (2005) 2093–2102.
[7] J. Canales-Vazquez, J.C. Ruiz-Morales, J.T.S. Irvine, W. Zhou, J. Electrochem. Soc. 152 (7) (2005) A1458–A1465.
[8] C. Brink, C. Kroeze, Z. Klimont, Atmos. Environ. 35 (2001) 6299–6312.
[9] M.R. Pai, A.M. Banerjee, K. Kartha, R.V. Pai, V.S. Kamble, S.R. Bharadwaj, J Phys. Chem. B 114 (2010) 6943–6953.
[10] F. Kapteijn, J.R. Mirasol, J.A. Moulijn, Appl. Catal. B 9 (1996) 25–64.
[11] P. Pomonis, D. Vatts, A. Lycourghiotis, C. Kordulis, J. Chem. Soc. Faraday Trans. 1 81 (1985) 2043–2051.
[12] A.K. Ladavos, P.J. Pomonis, Appl. Catal. B 2 (1993) 27–47.
[13] R.J.H. Voorhoeve, D.W. Johnson, J.P. Remeika, P.K. Gallagher, Science 195 (1977) 827–833.
[14] L.G. Tejuca, J.L.G. Fierro, J.M.D. Tascon, Adv. Catal. 36 (1989) 237–328.
[15] H. Tanaka, M. Misono, Curr. Opin. Solid State Mater. Sci. 5 (2001) 381–387.
[16] C.S. Swamy, J. Christopher, Catal. Rev. Sci. Eng. 34 (1992) 409–425.
[17] B. Viswanathan, Catal. Rev. Sci. Eng. 34 (1992) 337–352.
[18] M.R. Pai, A.M. Banerjee, S.R. Bharadwaj, S.K. Kulshreshtha, J. Mater. Res. 22 (2007) 1787–1796.
[19] M.R. Pai, B.N. Wani, N.M. Gupta, J. Mater. Sci. Lett. 21 (2002) 1187–1190.
[20] M.R. Pai, B.N. Wani, N.M. Gupta, J. Chem. Phys. Solids 67 (2006) 1502–1509.
[21] M.R. Pai, B.N. Wani, A.D. Belapurkar, N.M. Gupta, J. Mol. Catal. A: Chem. 223 (2004) 275–283.
[22] M.R. Pai, B.N. Wani, B. Shreedhar, S. Singh, N.M. Gupta, J. Mol. Catal. A: Chem. 246 (2006) 128–135.
[23] A.M. Banerjee, M.R. Pai, K. Bhattacharya, A.K. Tripathi, V.S. Kamble, S.R. Bharadwaj, S.K. Kulshreshtha, Int. J. Hydrogen Energy 33 (2008) 319–326.
[24] X.-H. Huang, J. Chang, Mater. Chem. Phys. 115 (2009) 1–4.
[25] Z. Qiu, Y. Zhou, M. Lu, A. Zhang, Q. Ma, Solid State Sci. 10 (2008) 629–633.
[26] H. Taguchi, Y. Masunaga, K. Hirota, O. Yamaguchi, Mater. Res. Bull. 40 (2005) 773–780.
[27] R.A. Nyquist, R.O. Kajel, Infrared Spectra of Inorganic Compounds, Academic Press, New York, 1971.
[28] D. Chen, X. Jiao, R. Xu, Mater. Res. Bull. 34 (1999) 685–691.
[29] J.T. Last, Phys. Rev. 105 (1957) 1740–1750.
[30] U. Balachandran, N.G. Eror, J. Mater. Res. 4 (1989) 1525–1528.
[31] M.T. Paques-Ledent, Spectrochim. Acta Part A 32 (1976) 1339–1344.
[32] P. Tarte, Spectrochim. Acta Part A 23 (1967) 2127–2143.
[33] W. Zheng, R. Liu, D. Peng, G. Meng, Mater. Lett. 43 (2000) 19–22.
[34] M. Abdelmola, M. Petitjean, G. Caboche, J.-M. Genin, L.C. Dufour, Hyperfine Interact. 156/157 (2004) 299–303.
[35] N.S. Gajbhiye, S. Bhattacharya, G. Balaji, R.S. Ningthoujam, R. Kumar Das, S. Basak, J. Weissmuller, Hyperfine Interact. 165 (2005) 153–159.
[36] M.R. Pai, K.K. Kartha, A.M. Banerjee, A. Bokare, R. Tewari, G.K. Dey, V.S. Kamble, S.R. Bharadwaj, 19th National Symposium on Catalysis (CATSYMP-19), held at National Chemical Laboratory, Pune, India, during Jan 18–21, 2009.